

Role of synoptic- and meso-scales on the evolution of the boundary-layer wind profile over a coastal region: the near-coast diurnal acceleration

Pedro A. Jiménez^{1,2} · Jordi Vilà-Guerau de Arellano³ · Jimy Dudhia⁴ · Fred C. Bosveld⁵

Received: 11 March 2015 / Accepted: 19 August 2015 / Published online: 7 September 2015
© Springer-Verlag Wien 2015

Abstract The contributions of synoptic- and meso-scales to the boundary layer wind profile evolution in a coastal environment are examined. The analysis is based on observations of the wind profile within the first 200 m of the atmosphere continuously recorded during a 10 year period (2001–2010) at the 213-m meteorological tower at the Cabauw Experimental Site for Atmospheric Research (CESAR, The Netherlands). The analysis is supported by a numerical experiment based on the Weather Research and Forecasting (WRF) model performed at high horizontal resolution of 2 km and spanning the complete observational period (10 years). Results indicate that WRF is able to reproduce the inter-annual wind variability but with a tendency to be too geostrophic. At seasonal scales, we find a differentiated behavior between Winter and Summer seasons with the Spring and Autumn transition periods more similar to the Summer and Winter modes, respectively. The winter momentum budget shows a weak intradiurnal variability. The synoptic scale controls the shape of the near surface wind profile that is characterized

by weaker and more ageostrophic winds near the surface than at higher altitudes within the planetary boundary layer (PBL) as a result of the frictional turning. In turn, during summer, mesoscale circulations associated with the differential heating of land and sea become important. As a result, the PBL winds show a stronger intradiurnal component that is characterized by an oscillation of the near surface winds around the geostrophic direction with the maximum departure in the afternoon. Although also driven by thermal land-sea differences, this mesoscale component is not associated with the classical concept of a sea-breeze front. It originates from the thermal expansion of the boundary layer over land and primarily differs from the sea-breeze in its propagation speed resulting in a wind rotation far ahead of any coastal front. We refer to it as the near-coast diurnal acceleration (NCDA). The contribution of the NCDA depends on the specific orientation of the coast (NE-SW at CESAR). Our findings stress the importance of evaluating and understanding the performance of mesoscale models with multi-year observational/simulated data sets in order to provide a statistically robust characterization of the limitations of surface layer and boundary-layer parameterizations and thus compensate for the scarceness of upper level wind observations.

Responsible Editor: S. Hong.

✉ Pedro A. Jiménez
jimenez@ucar.edu

¹ Research Applications Laboratory, National Center for Atmospheric Research, 3450 Mitchell Ln., Boulder, CO 80301, USA

² División de Energías Renovables, CIEMAT, Madrid, Spain

³ Meteorology and Air Quality Group, Wageningen University, Wageningen, The Netherlands

⁴ Mesoscale and Microscale Meteorology Division, National Center for Atmospheric Research, Boulder, CO, USA

⁵ Regional Climate Division, KNMI, De Bilt, The Netherlands

1 Introduction

The near surface winds present important deviations from the geostrophic balance that controls the synoptic winds of the free troposphere. The interactions of the atmosphere with the Earth's surface are ultimately responsible for the imbalance. The atmospheric boundary layer is created as a result of these interactions, and controls the transport of

momentum from the free troposphere to the surface where dissipation due to friction occurs. Unfortunately, relatively few wind observations are routinely acquired at heights higher than 10 m above ground level (agl) which constitutes a handicap to unraveling the physical mechanisms controlling the shape of the wind profile in the planetary boundary layer (PBL).

Long records of wind observations at meteorological towers have contributed to characterize the near surface wind profile (e.g., Crawford and Hudson 1973; Lange et al. 2004; Pena et al. 2010; Drechsel et al. 2012). For instance, Crawford and Hudson (1973) used one year of observations to inspect the diurnal wind variations at different heights up to 457 m above ground level. The authors found a stronger wind shear during the night and a more well mixed momentum during daytime. From a more applied point of view, Drechsel et al. (2012) analyzed one year of data recorded at different towers to inspect the characteristics of the wind at the most relevant heights for wind energy applications. Although one year can be considered a long period for certain analyses, it is not long enough to robustly analyze the seasonal variability, or physical processes that due to their weak magnitude require a statistical analysis of a large sample of data. A multi-year period of records is necessary for these purposes. Complementary to the lower PBL sampling provided by observations recorded at towers, wind profilers provide samples of the wind within the complete PBL (e.g. Levi et al. 2011; Baas et al. 2009; Sakazaki and Fujiwara 2010). Baas et al. (2009) used tower observations at the Cabauw Experimental Site for Atmospheric Research (CESAR) combined with wind profiler data to analyze the climatology of the low level jet. CESAR has a relatively flat topography and not very heterogeneous land surface which makes the site an ideal place to progress in our understanding of the PBL winds. However, the authors pointed out limitations of the wind profilers in providing comprehensive observations with numerous gaps in the time series depending on the atmospheric stability.

In view of the relative scarcity of upper-level wind observations (higher than 100 m), mesoscale models (Pielke 2002) become a plausible alternative to estimate the structure of the PBL wind profile. The models not only provide a higher spatial coverage than observations but also physically consistent meteorological fields which allows one to inspect the importance of different mechanisms in controlling the structure of the wind profile. In spite of the increasing complexity of the models, their ability to reproduce the wind profile with enough accuracy is still uncertain. A detailed comparison with observations is necessary to quantify their ability to replicate nature (e.g. Hurley and Luhar 2009; Shimada et al. 2011). Ideally, a multi-year observational period becomes necessary to

robustly evaluate the diurnal and seasonal evolution as well as the interconnection of scales in controlling the wind.

This research presents for the first time a semi-climatological experiment to explore the possibility of using mesoscale models, configured at high spatial resolution, as an alternative to complement wind profile observations. The study further deepens our understanding of the physical mechanisms determining the temporal evolution and the vertical distribution of the PBL wind profile at a coastal environment. For this purpose, we combine 10 years of observations at CESAR and a simulation performed with the Weather Research and Forecasting model (WRF, Skamarock et al. 2008) spanning the same temporal period at a horizontal resolution of 2 km. First, we discuss the ability of the model to reproduce the inter-annual variability and daily patterns at different levels from surface to 200 m. Additionally, we inspect whether there are different patterns in the wind diurnal variability between summer (June, July and August hereafter) and winter (December, January and February hereafter). Based on the satisfactory replication of the observed wind profile, we quantify the contributions of the different components of the momentum budget to understand the physical mechanisms determining the seasonal behavior of the PBL wind patterns. The proximity of the ocean to CESAR (48 km) makes it a convenient site to study the seasonal dependence of wind to mesoscale effects since it is expected that there is an influence of thermal forcing associated with the land–sea contrast mainly during spring and summer. Indeed, previous studies have used surface wind observations to show the occurrence of sea-breeze episodes in The Netherlands (van Delden 1993; Coelingh et al. 1998; Tijn et al. 1999; Wichink Kruit et al. 2004). The analysis allows for the detection of a diurnal oscillation of the PBL winds, and the linking of this to forcing associated with the land-sea thermal contrast. This dynamical feature is independent of the classical concept of a sea-breeze front and it is herein referred to as the near-coast diurnal acceleration (NCDA). The NCDA originates from the thermal expansion of the boundary layer over land, and primarily differs from the sea-breeze in its faster propagation speed (the speed of sound) resulting in a wind rotation far ahead of any coastal front. Finally, our analysis serves as a reference for future studies testing physical parameterizations, or potential modifications of the representation of land–atmosphere interaction processes in mesoscale models.

The article is organized as follows. The following section describes the observations as well as the WRF numerical and physical settings. Section 3 discusses the evaluation. Based on the good agreement to reproduce the inter-annual variability, annual and diurnal evolution of the wind profile found during the evaluation, Sect. 4 analyzes the 10-year model results to inspect the physical

mechanisms controlling the wind profile that lead to the identification of the NCDA. Finally, the conclusions are presented in Sect. 5.

2 Data

The wind profile observations were taken at the 213 m CESAR tower at Cabauw (The Netherlands) from 1 Jan 2001 to 31 Dec 2010. The original wind speed and wind direction data consist of 10-min averages recorded at 10, 20, 40, 80, 140 and 200 m agl. Relatively few studies have focused on the wind profile at CESAR, and have mostly analyzed microscale processes (e.g. Holtslag 1984; Verkaik and Holtslag 2006) or the shape of the wind speed distribution (Wieringa 1989). A description of the site and some boundary layer experiments can be found in van Ulden and Wieringa (1996) whereas Bosveld et al. (1999) evaluated ERA-15 over shorter temporal periods. Based on the hourly averaged wind observations, we herein inspect the wind behavior at CESAR at a range of temporal scales.

The simulation is performed with the WRF model version 3.4.1 (Skamarock et al. 2008). The model is configured with a total of four domains (Fig. 1). The outermost domain is centered at CESAR and is a square of about 3000 km. The horizontal resolution is 54 km. The rest are two-way domains interacting with a three to one spatial

refinement to progressively reach a horizontal resolution of 2 km over the region around CESAR. We use a standard distribution of vertical levels (36) imposing finer vertical resolution near the surface in order to replicate the distribution of the wind sensors (inset in Fig. 1). The first vertical level (the half level) is located at around 15 m agl to study the performance of the surface layer parameterization that is responsible for the diagnosis of the surface wind (10 m) from the first model level.

Initial and boundary conditions from the ERA-Interim reanalysis at $0.75^\circ \times 0.75^\circ$ (Dee et al. 2011) are prescribed to model the atmospheric evolution during the complete observational period. The numerical experiment consists of a series of short WRF runs. The model is initialized at the 0 UTC of each day and is run for 48 h recording the output every hour. The first day is discarded as a spin-up for the physical processes that are parameterized, and the simulation and results of the numerical experiment for the second day are retained as the simulation for that day. The process is repeated until obtaining one simulation for each day of the observational period (2001–2010). A similar downscaling methodology has been previously used to analyze the surface wind over complex terrain at a wide range of scales (e.g. Jiménez et al. 2011a, b, 2013). The modeling strategy adopted is especially suited for our research questions since it ensures that the atmospheric simulation will closely follow the synoptic scales. This is

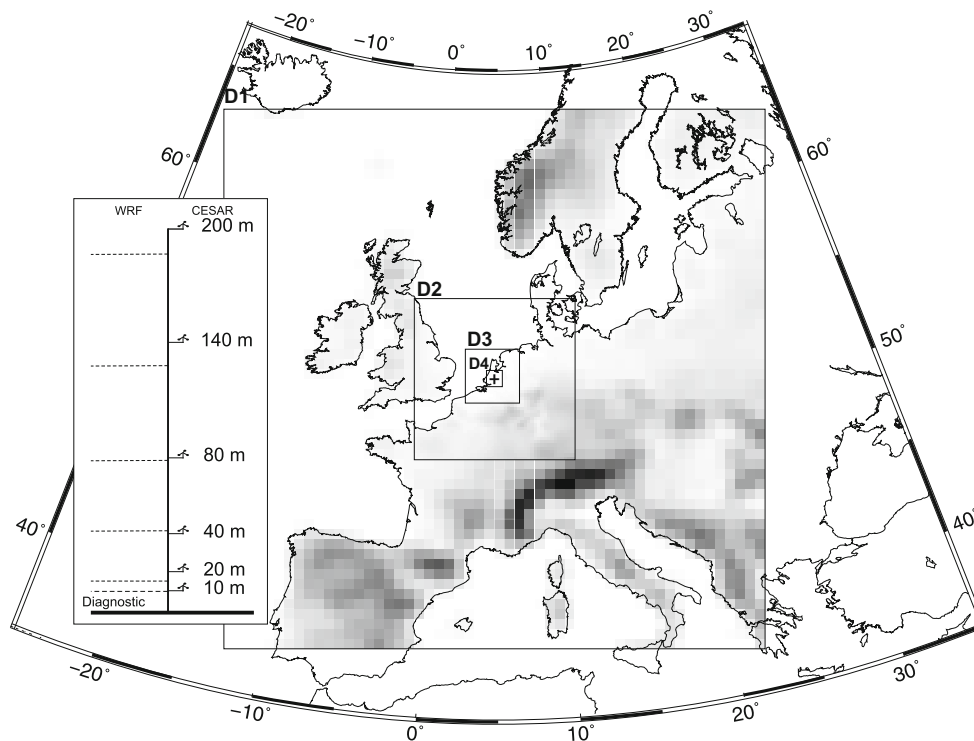


Fig. 1 The four domains used in the 10-year WRF numerical experiment. The elevation (shaded) and the vertical distribution of the levels closer to the ground (inset) are also shown. The plus symbol denotes the location of CESAR at the center of domain D4

crucial in our study where we attempt to encompass and represent a wide range of spatio-temporal scales that drive the momentum budget. The similar atmospheric evolution to the observed one relies on the re-initializations that keep the WRF evolution close to ERA-Interim atmospheric state, a blending of simulation with observations through an assimilation process. CESAR is located at about 1500 km from the nearest outer boundary, which indicates that an air parcel must travel at more than 8 ms^{-1} to reach CESAR at the end of a short WRF simulation (2 days). This is a good choice to keep the boundaries far enough to prevent the propagation of errors from the boundary conditions to the target location; and, at the same time, not too far to constrain the atmospheric evolution towards the ERA-Interim reanalysis. The interested reader is referred to Skamarock et al. (2008) for specific details in the treatment of initial and boundary conditions in WRF.

The effects of several physical processes are parameterized. The longwave and shortwave radiation fluxes follow Mlawer et al. (1997) and Dudhia (1989), respectively. The effects of microphysical processes are represented in the model with the WRF single-moment six-class scheme (Hong and Lim 2006). The effects of cumulus are only parameterized in the first three domains following Kain and Fritsch (1990, 1993). The Yon-Sei University PBL parameterization is the scheme used to represent the turbulent mixing transport. It is a first-order closure with the turbulent fluxes proportional to the gradients (K-theory), and a countergradient term to take into account the non-local mixing, and explicit entrainment fluxes (Hong et al. 2006). Finally, the land surface processes are simulated using a

5-layer model that diffuses the temperature in the ground keeping the soil moisture availability to its climatological values (Dudhia 1996) as a first step towards a dynamic soil moisture treatment which has been shown to be of relevance for the stable boundary layer (Bosveld et al. 2014). More details regarding the different physical options of the model can be found in Skamarock et al. (2008).

The modeled wind components are linearly interpolated from the model levels to the height of the wind sensors, except for the wind at 10 m that is directly diagnosed by the WRF surface layer component (Jiménez et al. 2012). The wind profile at the nearest grid point to CESAR is selected for comparison with observations. In order to precisely replicate the observational dataset, those modeled winds associated with missing observations (between 0.8 and 1.5 % depending on the level) were removed from the WRF dataset completing the data preparation process.

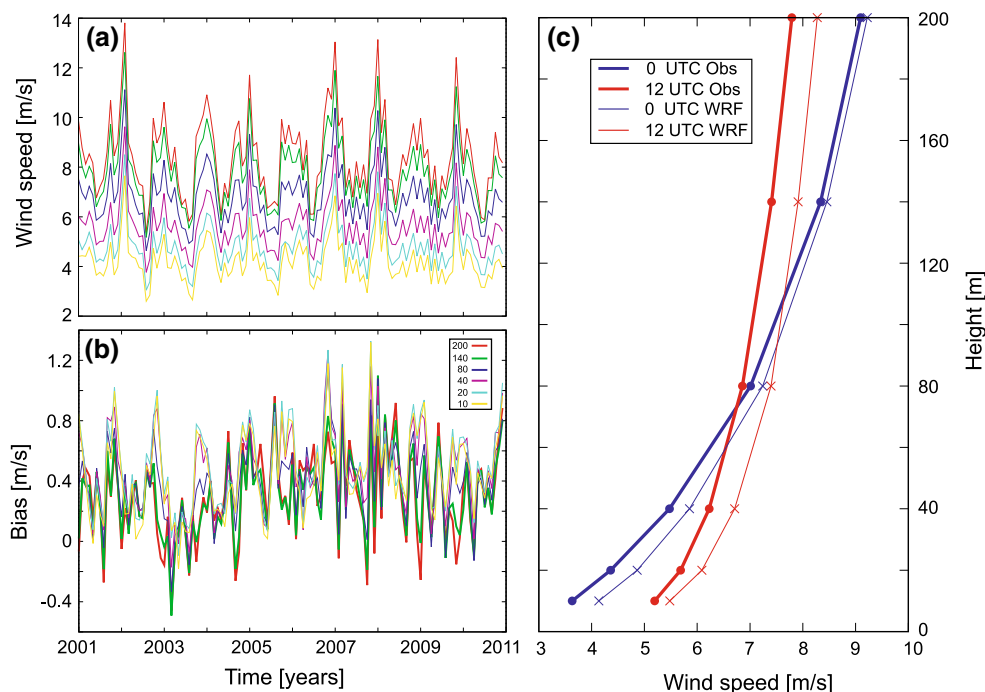
3 Evaluation

The following subsections present results for the wind speed (Sect. 3.1) and the wind direction (Sect. 3.2). A synthesis treating the wind as a vector that includes a physical explanation for the departures found is presented in the last subsection (Sect. 3.3).

3.1 Wind speed

The observed wind speed time series at the six levels averaged on a monthly basis are shown in Fig. 2a. The

Fig. 2 Observed monthly wind speed (a) and associated biases (model minus observations) (b) at the different levels (see legend in panel b for the respective heights). The observed and modeled mean wind speed profiles at 0 and 12 UTC calculated with data over the 10-year period (2001–2010) are also shown (c)



wind speed shows a noticeable vertical shear with a mean wind speed of 4.2 ms^{-1} (8.5 ms^{-1}) at 10 m (200 m) agl. Periods of maximum and minimum wind follow the annual evolution with higher (lower) winds during winter (summer). The annual amplitude is 1.8 ms^{-1} (3.9 ms^{-1}) at 10 m (200 m) agl. WRF reproduces these characteristics of the wind as shown by the small wind speed biases (Fig. 2b). However, the biases show a systematic behavior with a tendency to slightly overestimate the wind speed (0.4 ms^{-1}). Higher winds imply more variability (Jiménez et al. 2008); as a result, the mean absolute error progressively increases with height from 1.2 ms^{-1} at 10 m agl to 1.7 ms^{-1} at 200 m agl. The relative error is a more objective statistic to compare the estimations at the different levels and indicates a decrease of the error with height, ranging from 8.0 % at 10 m agl to 5.4 % at 200 m agl.

The fact that the biases are similar at different heights (Fig. 2b) indicates an adequate representation of the shape of the wind profile. This is further corroborated in Fig. 2c where we examine the mean wind speed profile at 0 and 12 UTC. WRF is able to reproduce the variation of the wind speed profile that occurs between stable (0 UTC) and unstable (12 UTC) situations. The tendency to overestimate

the wind speed is present under both stability conditions. The observed and simulated profiles are calculated with a large number of hours (always more than 3590) which lead to very small standard errors of the mean profiles. The overestimation of the wind is therefore statistically robust. It will be shown in Sect. 3.3 that the overestimation is associated with enhanced turbulent mixing. WRF also reproduces the increase of the variance with height (not shown), although consistent with the slight overestimation of the mean, it shows a slight overestimation of the variance which is always smaller than 13 %.

A more complete characterization of the annual evolution of the wind speed profile and wind speed biases including the influence of intra-diurnal variations is shown in Fig. 3. Observations at the surface present a clear diurnal evolution with higher winds during the day than during the night (Fig. 3e). Both, winter and summer seasons present this pattern but the diurnal amplitude is higher during the summer months. The wind speed at 80 m shows an attenuation of the surface pattern (Fig. 3c) but the diurnal variation is reversed at 200 m (Fig. 3a). The wind speed at 200 m is weaker during the day than during the night with weak diurnal variations during winter. The varying

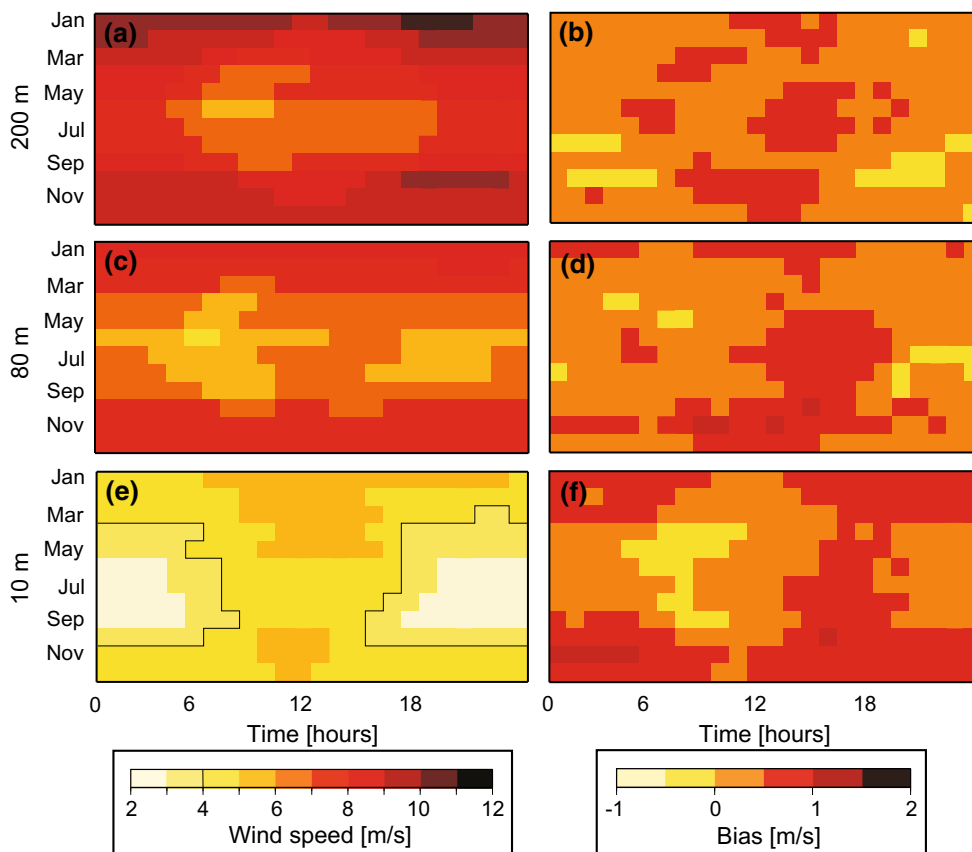


Fig. 3 Mean observed wind speed (left) and wind speed bias (right) as a function of the hour of the day and time of the year. Results for different heights agl are shown (rows)

behavior of the wind with height has been attributed to the combined influence of friction and turbulent mixing in the convective boundary layer (Crawford and Hudson 1973). The increase at the surface is related to the downward transport of momentum entrained from the free troposphere due to the PBL growth. The increase of the surface friction due to the higher surface winds is responsible for a reduction of momentum at higher levels in the PBL. The wind speed biases at the different heights are small which indicates that WRF reproduces the annual and intra-diurnal evolution of the wind profile (Fig. 3b, d, f). The larger departures occur during winter nights near the surface (Fig. 3f) and during convective conditions at upper levels such as 200 and 80 m (Fig. 3b, d) that show biases smaller than 1 ms^{-1} .

To conclude the analysis of the wind speed, Fig. 4 shows the diurnal variations of observed and modeled wind speed profile for winter and summer calculated with the 10-year data. As previously mentioned, the annual evolution is reproduced satisfactory as well as the diurnal wind variations. Larger differences appear for the lower part of the wind profile (10–40 m) with a tendency to overestimate the wind speed especially clear for winter (Fig. 4a, b). The diurnal evolution during the summer shows an interesting behavior at upper levels (height $\geq 80 \text{ m}$). Both observations and WRF show a minimum at first hours of the morning with a subsequent increase reaching a maximum in the afternoon. This behavior is explained in terms of the

diurnal cycle of the boundary layer height. The PBL is shallow during the morning (averaged value of 298 m at 7 UTC from the WRF simulation) and deeper in the afternoon (1024 m at 16 UTC). During the morning, the downward transport of momentum associated with the diurnal turbulent mixing increases the near surface wind at the expense of decreasing the wind near the top of the PBL, i.e., 200 m. In the afternoon, when the PBL reaches its maximum height, all the observational heights are within the lower part of the PBL, and thus the wind increases in all of them as a consequence of the downward turbulent transport of momentum from higher atmospheric layers in the PBL. The wind is still weaker than night at 200 m due to the effects of surface friction in the PBL. The effect is not seen in winter because the diurnal variation of the PBL height is small (less than 100 m between the stable boundary layer and the convective boundary layer).

3.2 Wind direction

The observed wind direction averaged on a monthly basis shows that the prevailing winds at the different levels are from the southwest (Fig. 5a). The monthly wind direction has been calculated averaging the observed wind vectors within each month and then computing the resulting mean direction. WRF shows a different performance in reproducing the wind direction at the different levels (Fig. 5b). The wind direction at 200 m agl shows a bias of 4° (relative

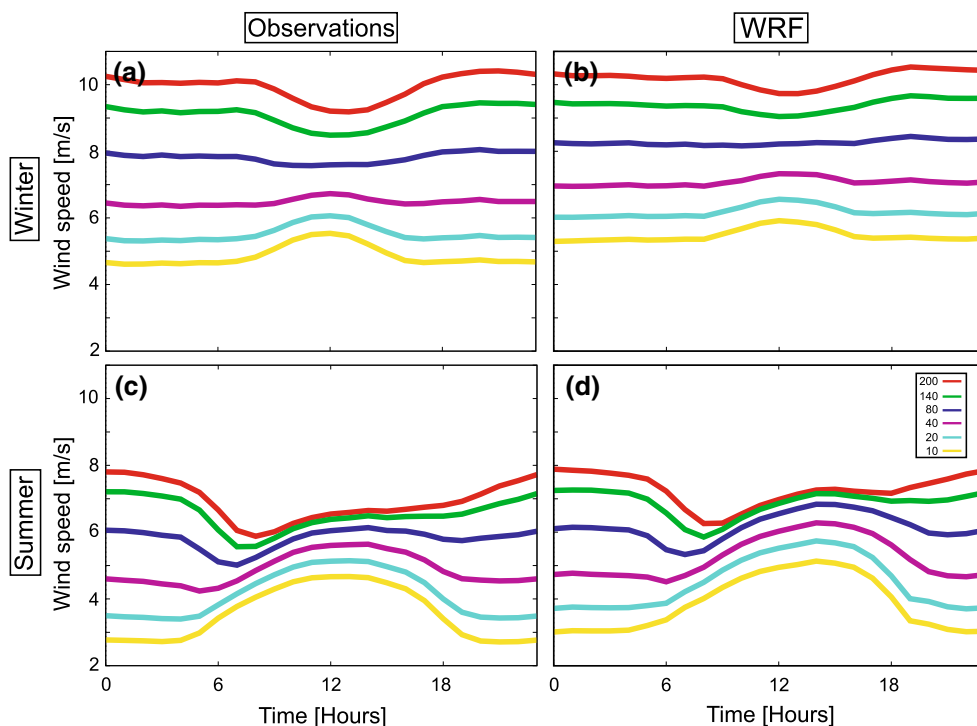


Fig. 4 Mean wind speed diurnal cycle at the different vertical levels (see legend) for winter (*first row*) and summer (*second row*). Both, the diurnal cycle calculated with observations (*first column*) and WRF (*second column*) are shown

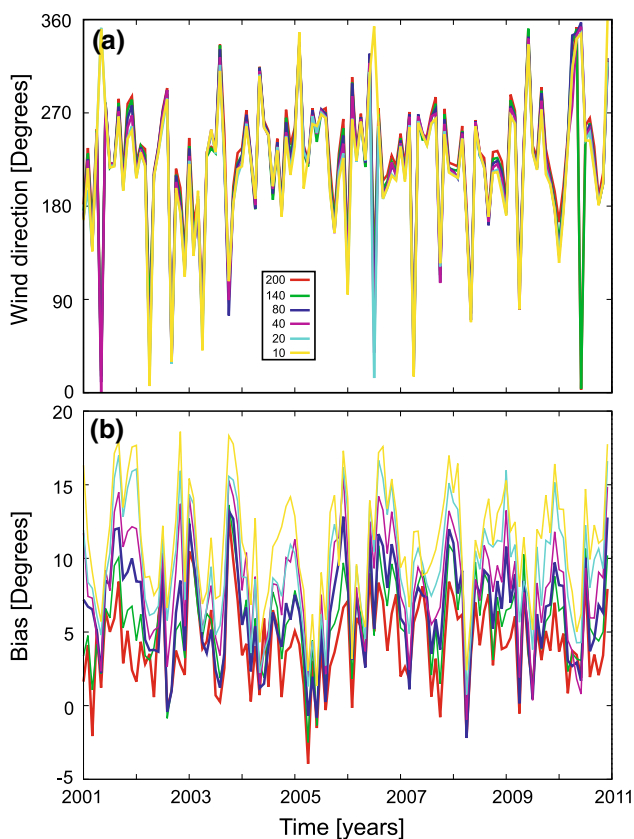


Fig. 5 Observed wind direction (a) and wind direction biases (b) at the different levels (see legend for the respective heights)

error of 2 % with respect to a maximum possible deviation of 180°). However, the wind direction bias at the surface is about 11° (6 %). The mean absolute error is also higher at the surface, ranging from 21° at 200 m to 27° at 10 m. Although the biases are not very large they show a systematic behavior. This is especially clear for the surface wind direction (yellow) that shows larger departures from observations in winter than in summer.

Figure 6 shows a complete characterization of the wind direction and wind direction biases as a function of the annual as well as the intra-diurnal evolution. Winter months show small diurnal variations of the wind direction profile (Fig. 6a, c, e). During Spring and Summer months, the variations are larger at the end of the afternoon. In particular, the winds are characterized by having an easterly component that has veered from northerly during the evening in Spring (especially April). This appears to be an unbalanced inertial turning of the ageostrophic wind from our momentum budget analysis (not shown). WRF captures these characteristics of the wind direction as revealed by the small bias magnitude in the wind direction profile (Fig. 6b, d, f). The highest biases appear near the surface and during stable situations and can be larger than 20° (11 %, Fig. 6f). The larger biases that take place in winter are partially associated

with the longer portion of the day with stable conditions (Fig. 6f). In addition, it will be shown that winter is characterized by a stronger influence of the synoptic situation than summer, when mesoscale phenomena become more important, and therefore this also contributes to the larger systematic deviations during winter months. At higher observational heights the biases decrease with values generally smaller than 10 or even 5° (e.g., 80 m, Fig. 6d). This confirms the differentiated skill of the model to reproduce the wind direction at different atmospheric layers.

To complete this analysis, we compare the observed and simulated veering of the wind with height. Figure 7 shows the difference between the wind direction at 200 m agl and the rest of the heights during the mean diurnal variations of winter and summer. The observations reveal that there is a lower wind veering during the day than during the night during both Winter (Fig. 7a) and Summer (Fig. 7c). Summer shows a weaker (stronger) veering during the day (night) than winter. These characteristics are reproduced by the modeled wind direction (Fig. 7b, d), with a tendency to underestimate the atmospheric turning during the night and to a lesser extent during the day.

The reason for the differentiated behavior of the diurnal evolution during winter/summer is likely due to the high turbulent mixing that occurs during the day in summer. On the one hand, the daytime turbulent mixing is weaker in winter leading to higher turning with height than summer. On the other hand, the large contrast between the strength of turbulent mixing during the day and night that takes place in summer leads to the higher diurnal amplitude.

3.3 Wind vector

The previous results have shown that WRF is able to reproduce notable characteristics of the wind profile within the first 200 m of the atmosphere. More specifically, the inter-annual variability, the annual evolution as well as the intra-diurnal variations are well reproduced by WRF. However, there is a systematic tendency to overestimate the wind speed and show positive biases of the wind direction. This indicates that the lower level wind profile is too geostrophic. This is associated either with (1) too much mixing or (2) too little friction with the surface. A comparison of the observed and simulated roughness length indicates that WRF overestimates it by about 0.02 (0.10) m in winter (summer) which points to the former, an enhanced turbulent mixing, as being responsible for the biases encountered. This hypothesis is reinforced by idealized simulations (not shown) that produce a reduction of the lower level wind speed as a result of decreasing the strength of the turbulent mixing (not shown).

The diurnal variations of the mean wind profile during winter (Fig. 8) and summer (Fig. 9) further quantifies these

Fig. 6 Wind direction (*left*) and wind direction biases (*right*) as a function of the hour of the day and time of the year at different heights agl

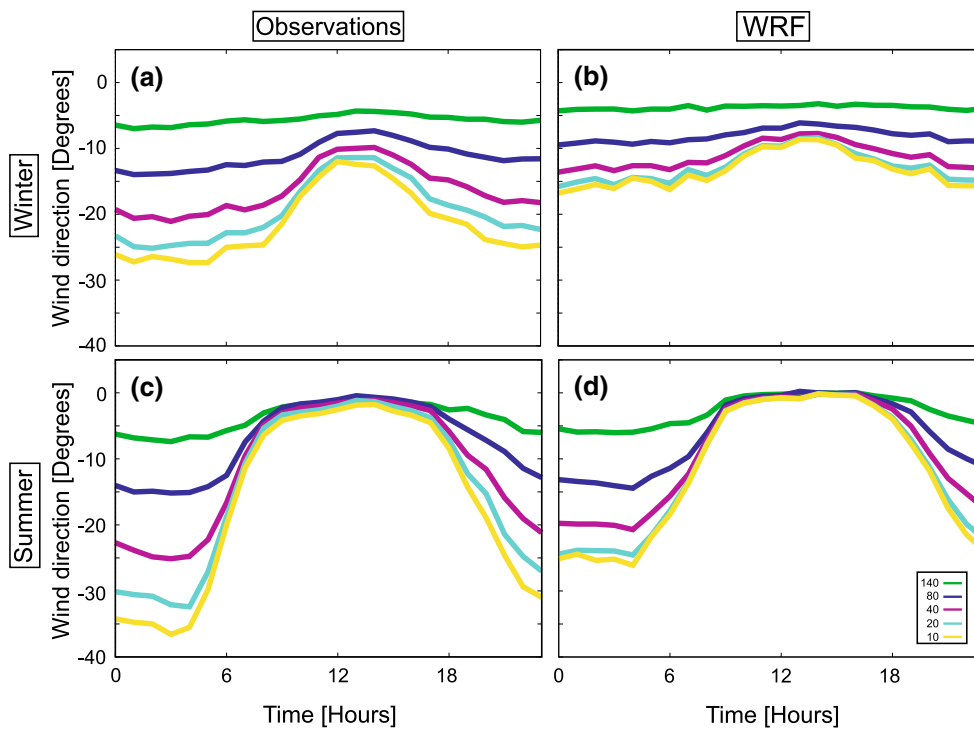
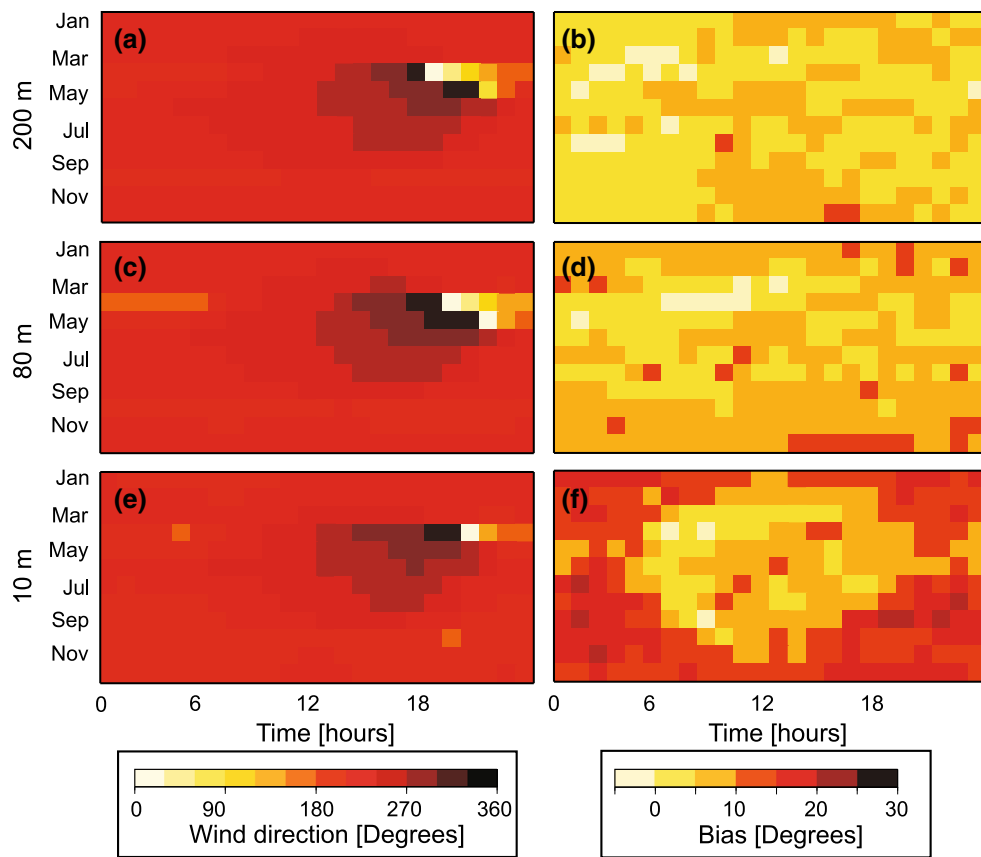


Fig. 7 Mean diurnal cycle of the wind direction differences between 200 m agl and the rest of the levels (see legend) for winter (*first row*) and summer (*second row*). Both, results for the observations (*first column*) and WRF (*second column*) are shown

Fig. 8 Mean wind profile at different hours during the winter. Observations (WRF results) are shown in *black* (*gray*). The first five modeled *arrows* correspond to the observational heights (10, 20, 40, 80, 120 and 200 m) whereas the rest of the *arrows* correspond to the wind at every 100 m up to a height of 4 km

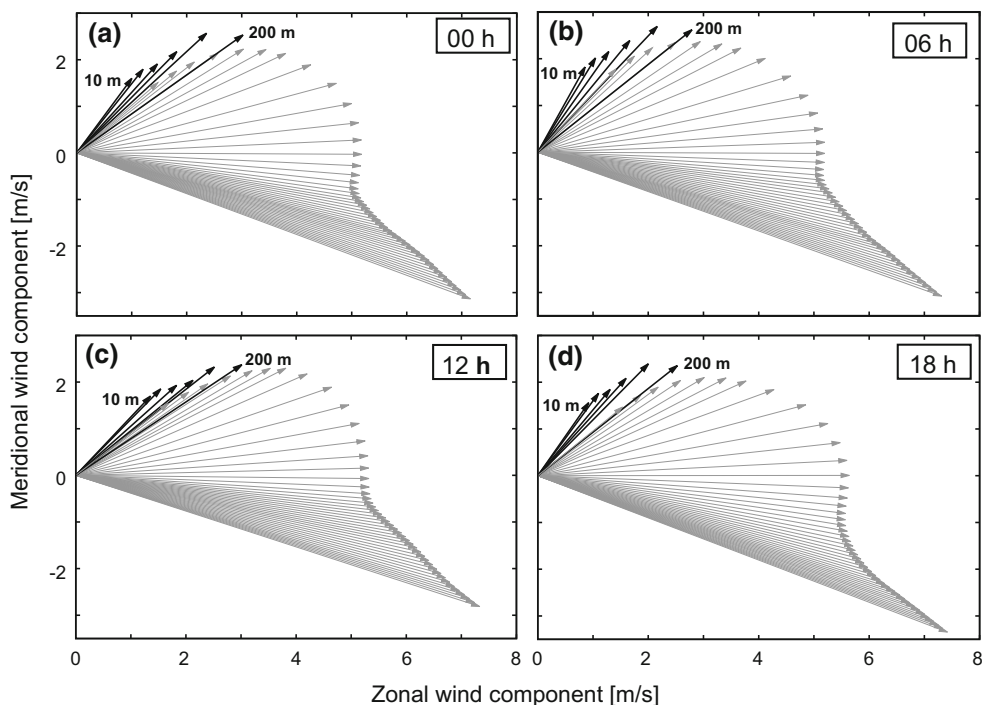
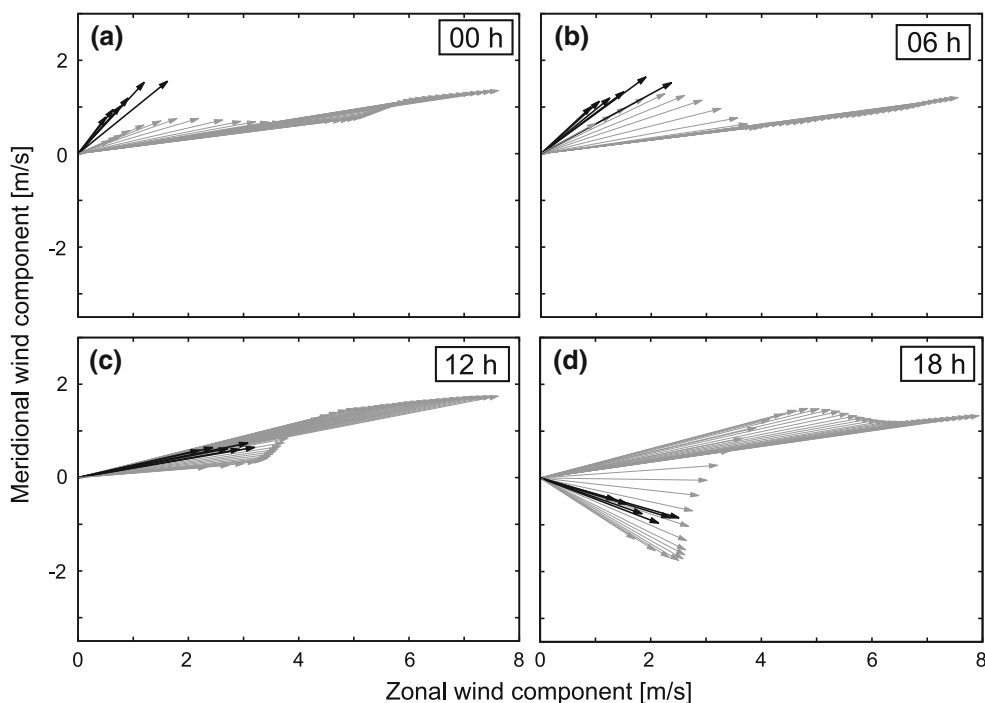


Fig. 9 Same as Fig. 8 but for Summer



characteristics. The winter wind profile shows small diurnal variations. The wind speed decreases with decreasing height backing to the left of the geostrophic wind direction. This pattern is associated with the effects of surface friction that introduces an ageostrophic component that causes the near surface winds to deviate from the geostrophic balance. Assuming a satisfactory replication of the geostrophic winds by WRF due to the frequent re-initializations, the

modeled surface winds do not vary as much as the observations showing slightly weaker departures during winter. This has been noticed in other models during stable conditions in an intercomparison study of single column simulations (Svensson and Holtslag 2009).

The diurnal variations during summer reveal an interesting oscillation of the wind around the geostrophic wind (Fig. 9). The oscillation is reproduced by WRF and is a first

indication that, during summer, mesoscale phenomena are becoming important and of similar order of magnitude as the synoptic scale. Actually, the mesoscale component modulates the synoptic influence that dominates during the winter season.

The overall positive comparison with observations motivated us to inspect the physical mechanism responsible for the wind oscillation in the following section.

4 Analysis of the momentum budget: identification of NCDA

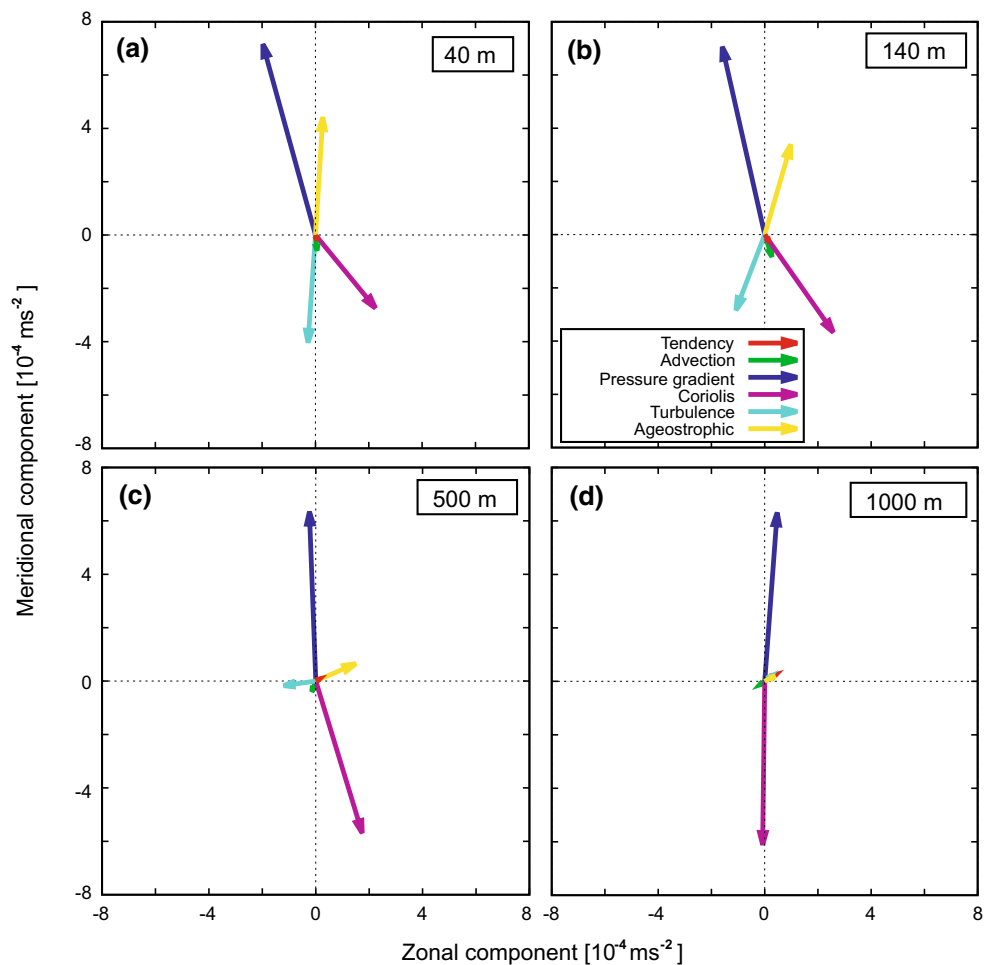
On the basis of the satisfactory replication of the observed wind profile by WRF, modeling results are herein used to inspect the contribution of the different components of the momentum budget to the wind profile structure. The equation for the conservation of momentum for the zonal wind component (u) in Einstein's summation notation reads

$$\frac{\partial \bar{u}}{\partial t} + \bar{u}_i \frac{\partial \bar{u}}{\partial x_i} = -\frac{1}{\bar{\rho}} \frac{\partial \bar{p}}{\partial x} + f\bar{v} - \frac{\partial \overline{u'u'_i}}{\partial x_i} \quad (1)$$

where the over bars indicate mean quantities and the primes departures from the mean. The index i in the advection and turbulent terms goes from 1 to 3 being $u_1 = u$, $u_2 = v$ and $u_3 = w$ the zonal, meridional, and vertical wind components, respectively; f is the Coriolis parameter, p represents the pressure, and ρ is the air density. The first term on the left hand side represents the local change in zonal wind whereas the second one represents advection. The first term on the right hand side is the contribution of the mean pressure gradient force; the second one is the Coriolis force; and the last one is the divergence of the momentum flux that represents the effects of turbulent mixing. An analogous expression holds for the meridional wind component but with the reversed sign for the Coriolis force.

The different terms of the momentum budget (Eq. 1) are computed using the hourly outputs of the model. The calculation of the terms representing the advection, the Coriolis force and the pressure gradient force is straightforward. The local changes or tendencies are calculated using two consecutive WRF outputs; and, finally, the

Fig. 10 Mean components of the momentum balance (see Eq. 1) at different heights calculated with the winter data at 12 UTC. The red arrow represents the tendency whereas the rest of the arrows represent the contribution to the tendency of the different physical processes (see legend). The ageostrophic contribution is defined as the contribution of the Coriolis term plus the pressure gradient one



turbulent mixing contribution is computed as the residual. This term includes the frictional effects and the entrainment of momentum at the inversion zone.

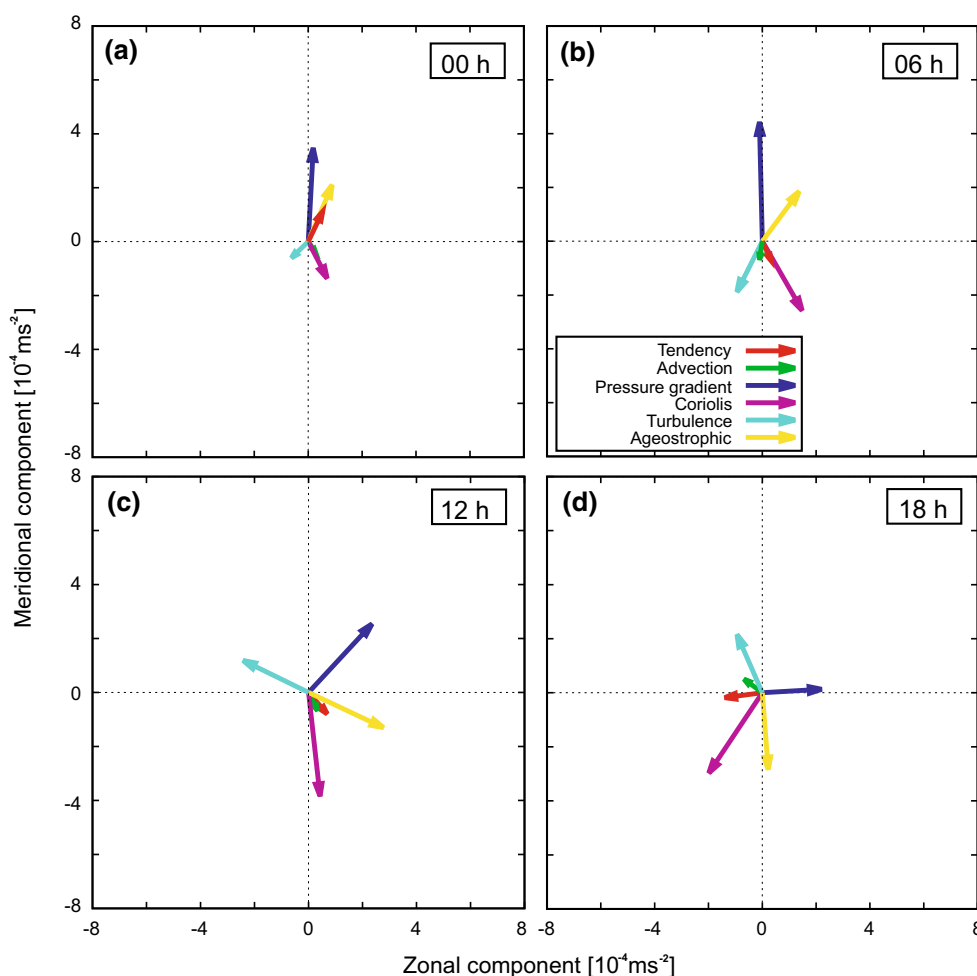
Figure 10 shows the contribution of the different components of the momentum balance calculated with the winter data at 12 UTC. At 1000 m the pressure gradient force (dark blue arrow) and the Coriolis force (purple arrow) are close to balance indicating that the winds are geostrophic at this level (Fig. 10d). Closer to the surface, at 500 m, the ageostrophic term (defined as the sum of the Coriolis force and the pressure gradient force) increases its value (Fig. 10c) being even higher at 140 m (Fig. 10b) and at 40 m (Fig. 10a). The ageostrophic contribution is mostly balanced with the contribution of the turbulence term, this last one being dominated by the surface momentum flux which is mainly friction. The pressure gradient contribution shows small deviations with height being close to the synoptic values at 1000 m. A similar vertical structure was found during the rest of the hours of the day consistent with the similar vertical profiles that takes place during winter (Fig. 8).

During summer, the momentum balance presents important differences with respect to winter. At 1000 m, it

shows a similar pattern during the diurnal evolution with the winds near geostrophic balance (not shown) that leads to the prevailing westerly winds (Fig. 9), but closer to the surface the different components show an interesting diurnal evolution. Figure 11 shows the momentum balance at 140 m at four different hours. The different contributions of the components ultimately respond to variations in the pressure gradient term (dark blue arrow). During the night it is oriented to the north (Fig. 11a, b) in the direction of the synoptic pressure gradient like the one at 1000 m. However, during the day it begins to veer clockwise (Fig. 11c) being completely oriented to the east at 18 UTC (Fig. 11d). The balance at other vertical levels shows a similar diurnal evolution to this pattern decaying almost linearly with height through the PBL (not shown). The wind and other forces rotate by a similar angle governed by this pressure rotation.

To corroborate this finding, we calculate the spectral analysis of the zonal and meridional pressure gradients using the 10-year simulated data. The stronger contribution of the diurnal component during summer becomes evident (Fig. 12). Both the zonal and meridional contributions do

Fig. 11 Mean components of the momentum balance (see Eq. 1) at 140 m at different hours for Summer. The red arrow represents the tendency whereas the rest of the arrows represent the contribution to the tendency of the different physical processes (see legend). The ageostrophic contribution is defined as the contribution of the Coriolis term plus the pressure gradient one



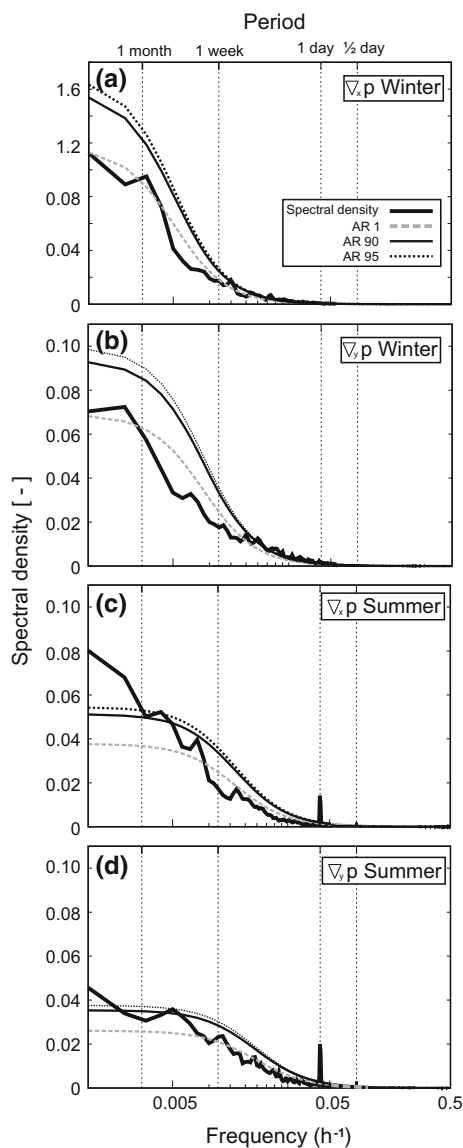


Fig. 12 Normalized spectral density of the zonal and meridional pressure gradient at 140 m for summer and winter (black thick lines), the first-order autoregressive process spectra (gray dashed lines), and the 90 % (black thin lines) and 95 % (black dotted lines) confidence limits

not show a significant difference with respect to an autoregressive process of order 1 during winter (Fig. 12a, b). However, during summer, both components show a significant contribution around the 1-day period (Fig. 12c, d). Ultimately, this diurnal contribution is associated with the more relevant role played by mesoscale phenomena that is superimposed on the contribution of the synoptic scale. In the following we provide an explanation of the physical mechanism driving the enhancement of the mesoscale component.

A plausible attribution is the contrast between the land and the sea temperatures that has been shown to be responsible for developing sea breezes in The Netherlands

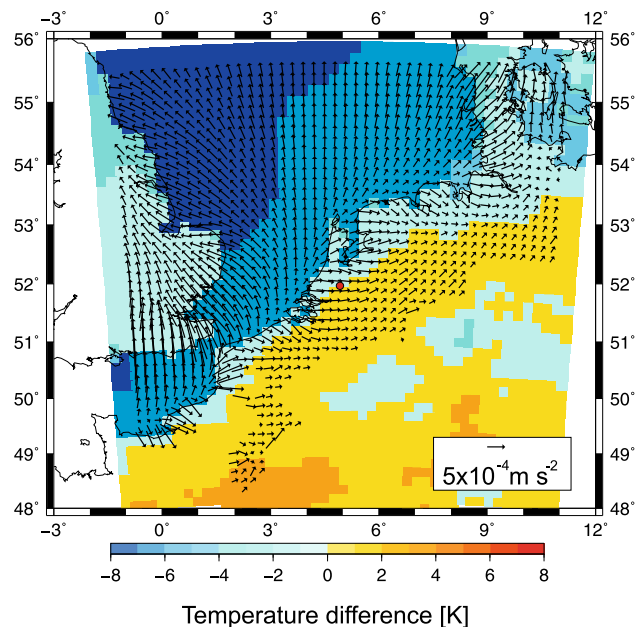
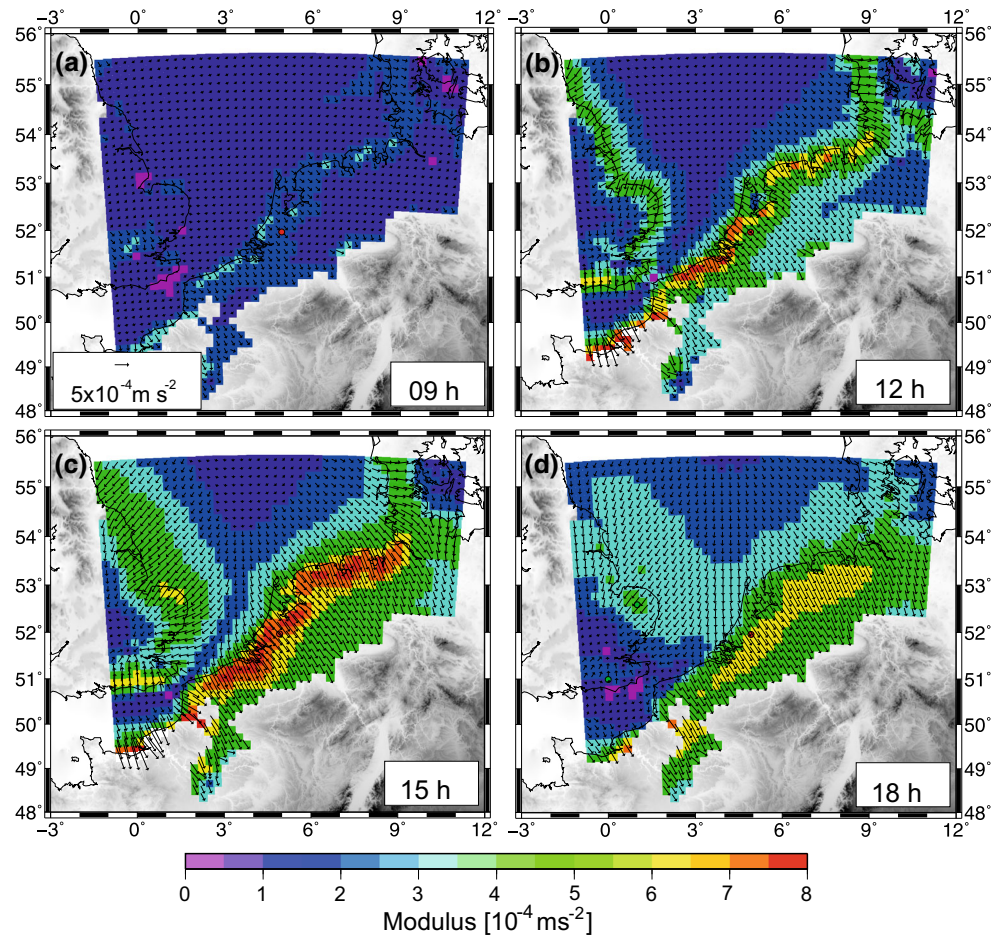


Fig. 13 Mean skin temperature differences with respect to CESAR (red circle) for summer at 15 UTC (shaded). The horizontal pressure gradient force (ms^{-2}) at 140 m is also shown (vectors)

(e.g., van Delden 1993; Wichink Kruit et al. 2004). The difference between the simulated skin temperature at CESAR and the one at the rest of the grid points in domain 2 (see Fig. 1) at 15 UTC during summer is shown in Fig. 13. There is a strong contrast between the ocean and land temperatures, the ocean points being colder than the land points by more than 2 K. This results in a pressure gradient force from the ocean to the land (arrows). The inland pressure gradient becomes evident at all the coast locations within domain 2 (Fig. 1) that show quite different directions due to the different coastal orientation (Fig. 13).

The effects of this mesoscale component, herein referred to as the NCDA, are quantified in Fig. 14 that shows the diurnal evolution of the pressure gradient at 140 m minus the one at 1000 m at 0 UTC. The structure of this pattern reflects the contribution of the mesoscale since the effects of the synoptic scale are removed by subtracting the contribution at 1000 m. It is implicitly assumed that the synoptic contribution does not vary with height which is supported in a subsequent analysis (Fig. 15 and related discussion). The differences are weak during the night, but start to show important contributions in coastal sites at 9 UTC (Fig. 14a). The mesoscale component is well developed at 12 UTC, with noticeable effects in all the coastal sites of the domain (Fig. 14b). At 15 UTC, the differences reach their maximum with values higher than $8 \times 10^{-4} \text{ms}^{-2}$ in northern mainland Europe including the CESAR site (Fig. 14c). Note that the magnitude of this pressure gradient is comparable with the mean synoptic-scale

Fig. 14 Pressure gradient (ms^{-2}) anomalies at 140 m with respect to 1000 m at 0 UTC (*arrows*) averaged for summer days at **a** 9 UTC, **b** 12 UTC, **c** 15 UTC and **d** 18 UTC. The modulus of the pressure gradient is highlighted (*shaded*). Elevation is also shown (*shaded gray*)



gradient. Three hours later, at 18 UTC, the mesoscale contribution begins to decay in favor of the synoptic contribution (Fig. 14d). During the night, the mesoscale contribution is very weak and there is no clear onshore or offshore component at any level.

The vertical structure of the simulated mesoscale component, NCDA, at CESAR is shown in Fig. 15. The mesoscale contribution is very weak during the night hours (Fig. 15a, b) but then the wind shows a clockwise rotation at low levels by 12 UTC (Fig. 9c) while the mesoscale pressure component shows a linear intensification maximizing towards the surface (Fig. 15c). At 18 UTC the wind veering is more intense as a consequence of the further intensification of the mesoscale component near the surface to the detriment of the effect of synoptic one (Fig. 15d).

The fact that the inland pressure gradient is noticeable hundreds of km inland (Fig. 14c) indicates that the mean mesoscale behavior does not rely on the formation of a sea breeze that shows typical penetrations of O (10 km). In addition, sea-breeze fronts are only occasionally identified over the The Netherlands and one should not expect an infrequent phenomenon to produce a mean climatological

impact and, even less plausibly, one of the large magnitude shown on Fig. 14. The rotation responds to the thermal contrast between land and ocean but is not dominated by the effects of the classical concept of a sea-breeze front that has a marked contrast of temperature and moisture after the frontal passage (Simpson et al. 1977). This is also deduced from the presence of the inland pressure gradient at CESAR for weak winds, and from the observations, that rarely show the sharp changes in temperature and moisture.

To analyze the origin of the NCDA, Fig. 16a shows the mean hour-to-hour change of the sea level pressure relative to the mean change at each hour for a number of locations in a section perpendicular to the coast (circles in Fig. 16b). During the sunrise, hours from 4 to 6 UTC, the pressure starts to decrease (increase) at far-inland (ocean) locations creating the mesoscale pressure gradient near the coast. This rapid development over a large area (350 km from point 1 to 10) is driven by horizontally propagating sound waves. These originate from the initial pressure gradient at the coast that results from the expansion of the boundary layer over land due to diabatic heating. Based on the analysis of one month's observations, van Delden (1993)

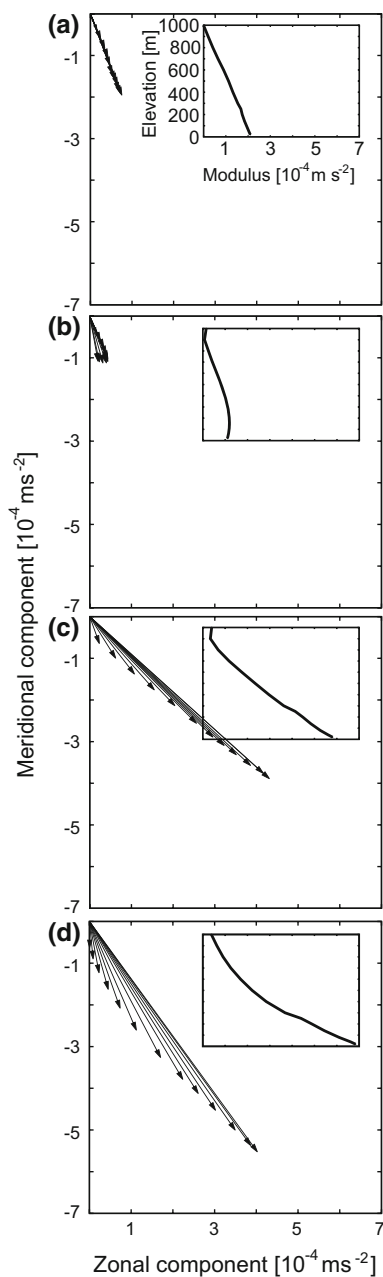


Fig. 15 Profile of the modeled pressure gradient at CESAR minus the one at 1000 m (*arrows*) for **a** 0 UTC, **b** 6 UTC, **c** 12 UTC and **d** 18 UTC. The *inset panels* represent the modulus of the pressure gradient differences as a function of elevation. For clarity, the labels of the *inset figures* are only shown in **a**

has shown that the pressure decrease over land is correlated with, and results from, diabatic boundary-layer heating. A similar plot to Fig. 16a but for observations, accompanied by idealized numerical simulations, by Tijm and van Delden (1999) has shown that this is the main mechanism for the sea-breeze initiation over the same region. For inland locations, we additionally find that the wind responds immediately to the change in the pressure gradient

introducing the rotation that has been shown herein to occur at CESAR. To distinguish from the sea breeze we refer to this mesoscale phenomena as the NCDA. Figure 16b shows the gradual increase of the pressure changes parallel to the coast (12 UTC) that ultimately leads to the mesoscale pressure gradient. Idealized simulations performed with WRF confirmed that the model is able to reproduce the horizontally propagating sound waves that led to the rotation of the winds herein described. To conclude this analysis, it is of interest to also notice the presence of a weak pressure rise propagating inland (points 4, 5, and 6 in Fig. 16a). The signal reaches CESAR by about 15 UTC and it is hypothesized to be related to the interaction of cold advection from the ocean with the diurnal cycle being a separate slower phenomenon than the NCDA.

The rapid intensification of the pressure gradient and the subsequent wind rotation are quantified in Fig. 17 that shows the pressure gradient and the surface winds as a function of the hour and the locations perpendicular to the coast. The inland rotation of the pressure gradient starts after 6 UTC (Fig. 17a). By 12 UTC, the pressure gradient direction has rotated almost 90° from the north-south direction and is almost parallel to the coast. The winds respond immediately even more than 100 km inland after 6 UTC, and show the veering as they become more north-westerly after the middle of the day (Fig. 17b). This is accompanied by an inland acceleration as the wind rotates through the WSW geostrophic direction around 12 UTC (see also Fig. 9c for Cabauw).

The rotation of the pressure gradient, that induces the acceleration/rotation of the winds, is, therefore, a result of the combined contribution of the synoptic and mesoscale pressure gradients. Figure 18 shows a sketch that conceptualizes the combined contribution. Assuming that the synoptic contribution is constant during the day and that the mesoscale contribution increases, the pressure gradient rotates clockwise. This explains the modeled behavior at CESAR during summer (Figs. 11, 17). The mechanism is simple one where the growing mesoscale pressure gradient over a large coastal area adds vectorially to the synoptic one. In this way, the originally synoptic pressure gradient will be modified during the day in the direction of the mesoscale gradient. It should be kept in mind that we are analyzing only average patterns that can be masked by rare situations such as where a decoupling with the surface occurs and leads to an inertial oscillation of the winds (Baas et al. 2009; Schröter et al. 2013).

In generalizing our findings, it is worth noting that the contribution of the mesoscale (NCDA) depends on the specific orientation of the coast. For example, it is from the east on the eastern side of the United Kingdom or from the south or the north in the English Channel (Fig. 14). As a

Fig. 16 **a** The mean changes in sea level pressure from hour to hour relative to the mean change at each hour at 10 points marked with a circle in **b**. A 3-h smoothing was applied to the time series. Data from the 10 summers (2001–2010) has been used. The sea level pressure changes over the complete domain at 12 UTC are also shown (**b**). The letter C in **b** denotes the location of CESAR

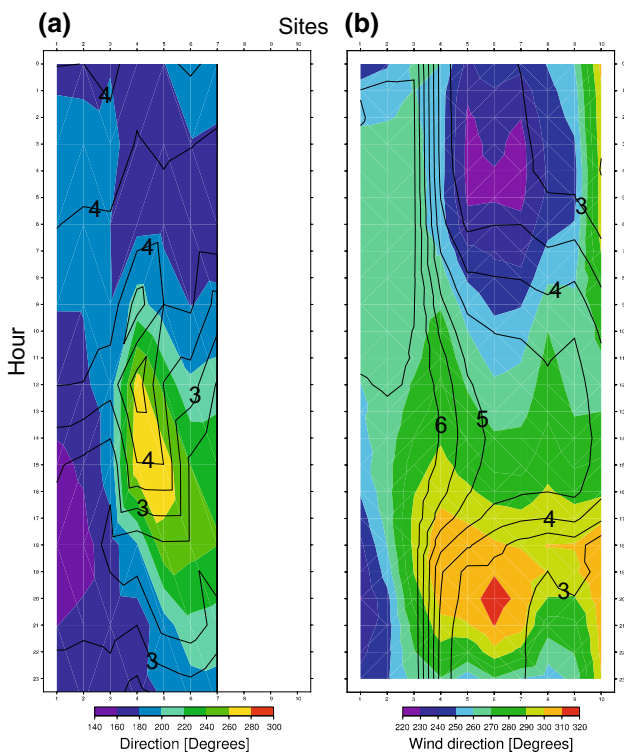
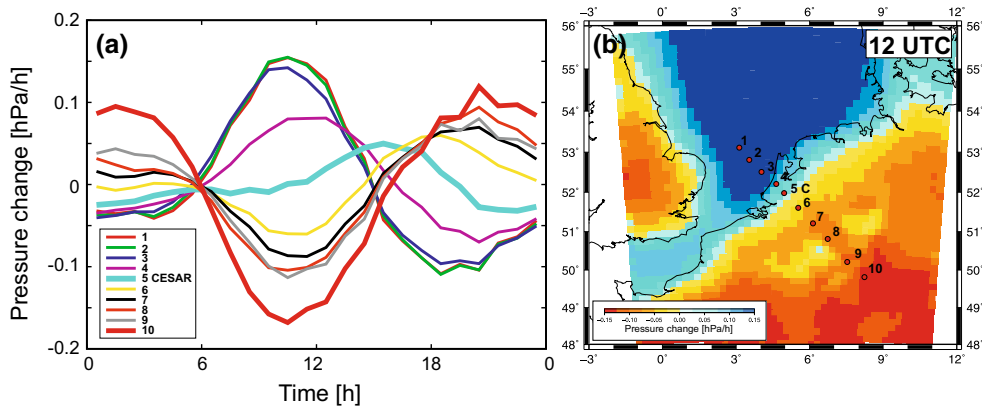


Fig. 17 **a** Pressure gradient at 140 m and **b** surface wind as a function of the hour of the day and the location (same sites as in Fig. 16). The direction is represented with colors (shaded) and the module with contour lines. The units are ms^{-1} for the wind speed and 10^{-4}ms^{-2} for the pressure gradient

result, the wind oscillation around the geostrophic wind introduced by the mesoscale component depends on the orientation of the coast line. Figure 19 shows the diurnal variation of the wind at several coastal locations within domain 2 calculated with the summer results for the 10 years. The sites located in northern mainland Europe show similar oscillations to the one observed at CESAR (red dot in Fig. 19) since the coast orientation is similar at these locations. The wind at these sites has a southward rotation during the day. However, the two locations in the United

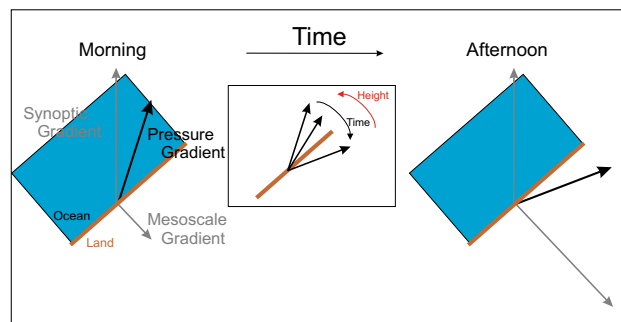


Fig. 18 Diagram showing the relative contribution of the synoptic and mesoscale pressure gradient at CESAR during the spring and summer seasons. The brown line represents the coast

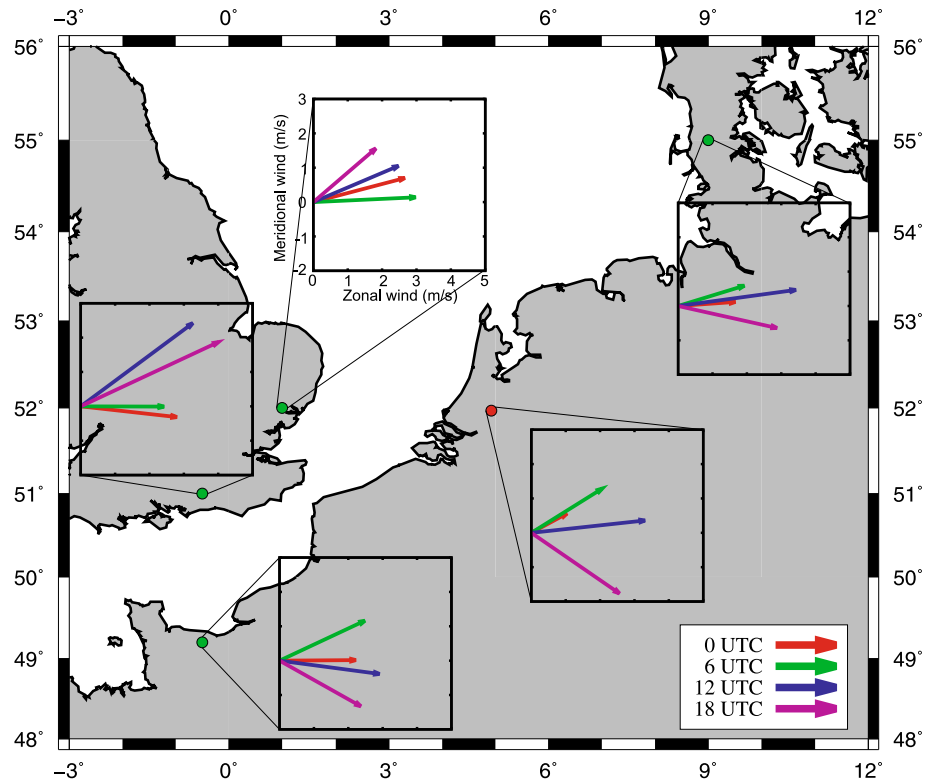
Kingdom show the opposite behavior. Diurnal hours present a northward rotation reflecting the dependency of the mesoscale contribution on the coast orientation.

5 Conclusions

A 10-year period of observational records combined with fine spatial mesoscale modeling enabled us to understand the wind profile near a coastal zone. The extended period of analysis allowed us to reach statistically robust conclusions regarding the model performance. Although with a tendency to be too geostrophic, WRF modeled winds reproduce the most important observed characteristics of the inter-annual variability, annual and diurnal evolution of the wind profile. Reducing the strength of the turbulent mixing during both stable and unstable conditions is necessary to provide better agreement between the observed and simulated winds. This conclusion applies for both the PBL wind profile and the diagnosis of the surface wind (10 m agl) by the surface layer parameterization.

A differentiated behavior was found during winter and summer with the modeled winds being able to capture these patterns. The analysis of the momentum budget

Fig. 19 Mean wind at 140 m at selected sites and hours (0, 6, 12 and 18 UTC) calculated with the WRF winds during the 10 summers



reveals important differences between these seasons. During winter, the contribution of the synoptic scale and the effects of the surface friction explain the vertical structure of the winds. In turn, during summer, there is an important mesoscale contribution, introduced by the surface thermal contrast between the land and the nearby ocean, NCDA, that competes with the synoptic scale and perturbs the momentum budget and therefore the winds. In particular, NCDA introduces an oscillation of the lower PBL winds. This contribution reaches its maximum magnitude at CESAR during the afternoon. The strength of the mesoscale contribution strongly depends on the height above ground with the maximum contribution nearest the surface. An important conclusion of this work is that NCDA is not associated with the classical concept of a sea-breeze front. Its influence on the pressure gradient is spread much more rapidly by sound waves. In turn, the rotation of the winds related to NCDA responds to the thermal contrast between land and ocean, that produces a reduction (increase) of the surface pressure over land (ocean) as a consequence of the thermal expansion of the boundary layer over land. Modeling results indicate a dependency of the oscillation on the coastal orientation. It should be emphasized that the detection of this mesoscale phenomena, NCDA, has been possible due to the extended period of analysis, 10 years, that allowed us to isolate the regional signal related to the differential heating of the Earth's surface.

This work ties together some previous concepts related to near-coastal circulations. Observational work by Mass (1982) noted diurnal coastal effects in the mean surface wind behavior in spring and summer, and suggested that they were due to both the land-sea contrast and complex terrain in Washington state. Sakazaki and Fujiwara (2008) used 14 years of June-July-August soundings in Japan to infer mean surface hodograph rotation rates and directions and also proposed that the basic effects were diurnal pressure gradients associated with both the land-sea contrast and nearby orography, creating a simplified diurnal model of pressure variation at a given site to demonstrate the effect. As in this study, these studies were related to long-term average coastal diurnal behaviors in the wind. Tijn et al. (1999) noted the pressure signal and its propagation from the coast at the speed of sound during sea-breeze cases, but their focus was on the winds associated with the sea breeze front rather than any larger-scale rotation. Here we have demonstrated with long-term mesoscale modeling that these surface pressure gradients that spread rapidly from the coast due to differential diurnal heating are responsible for the diurnal wind rotation in the spring to summer season even far ahead of any coastal front. The mesoscale model has been used to quantify the forces involved and detailed the vertical structure of this effect. The mechanism as described should be ubiquitous in environments of differential heating, and can be applied to

other coastal orientations and other relative sizes and directions of synoptic pressure gradients. A similar diurnal effect is likely to be found in the vicinity of orography where a pressure gradient may propagate rapidly into the plains and cause a turning.

Although the focus has been placed on inland locations, it is interesting to note that the contribution of the modeled mesoscale component associated with NCDA is also noticeable over the ocean (e.g., Fig. 14c). This is interesting to stress due to the difficulty of observing the wind over the ocean. The presence of this oscillation over the ocean is interesting not only from a theoretical point of view but also from a more applied one. There is a large development of offshore wind farms in the North Sea that are located near the coast. The sites selected for wind energy exploitation are, therefore, located in the region that presents the oscillation of the winds during summer. A detailed examination of available observations over the ocean should be made to confirm this modeling result. Mesoscale models, therefore, have a strong potential to compensate for the scarcity of observations and enable us to gain further understanding of the wind at different temporal and spatial scales.

References

- Baas P, Bosveld FC, Klein Baltink H (2009) A climatology of nocturnal low-level jets at Cabauw. *J Appl Meteorol Climatol* 48:1627–1642
- Bosveld FC, van Ulden A, Beljaars A (1999) A comparison of ECMWF re-analysis data with fluxes and profiles observed in cabauw. Tech. Rep. 8, ECMWF Re-Analysis (ERA) Project Report, ECMWF
- Bosveld FC, Baas P, Holtslag A, Angevine WM, Bazile E, Brujn ED, Decau D, Edwards JM, Ek M, Larson VE, Malardel S, Pleim JE, Raschendorfer M, Svensson G (2014) The third GABLS intercomparison case for boundary layer model evaluation. part b: results and process understanding. *Bound Layer Meteorol* 152:157–187
- Coelingh J, van Wijk AJM, Holtslag AAM (1998) Analysis of wind speed observations on the North Sea coast. *J Wind Eng Ind Aerodyn* 73:125–144
- Crawford KC, Hudson HR (1973) The diurnal wind variation in the lowest 1500 ft in central Oklahoma: June 1966–May 1967. *J Appl Meteorol* 12:127–132
- Dee DP, Uppala SM, Simmons AJ, Berrisford P, Poli P, Kobayashi S, Andrae U, Balmaseda MA, Balsamo G, Bauer P et al (2011) The ERA-Interim reanalysis: configuration and performance of the data assimilation system. *Q J Roy Meteorol Soc* 137:553–597
- Drechsel S, Mayr GJ, Messner JW, Stauffer R (2012) Wind speeds at heights crucial for wind energy: measurements and verification of forecasts. *J Appl Meteorol Climatol* 51:1602–1617
- Dudhia J (1989) Numerical study of convection observed during the winter monsoon experiment using a mesoscale two-dimensional model. *J Atmos Sci* 46:3077–3107
- Dudhia J (1996) A multilayer soil temperature model for MM5. Preprints, Sixth PSU/NCAR Mesoscale Model Users' Workshop, Boulder, CO 80307, pp 49–50
- Holtslag AAM (1984) Estimates of diabatic wind speed profiles from near-surface weather observations. *Bound Layer Meteorol* 29:225–250
- Hong SY, Lim JOJ (2006) The WRF single-moment 6-class microphysics scheme (WSM6). *J Korean Meteorol Soc* 42:129–151
- Hong SY, Noh Y, Dudhia J (2006) A new vertical diffusion package with an explicit treatment of entrainment processes. *Mon Wea Rev* 134:2318–2341
- Hurley P, Luhar A (2009) Modelling the meteorology at the Cabauw tower for 2005. *Bound Layer Meteorol* 132:43–57
- Jiménez PA, González-Rouco JF, Montávez JP, Navarro J, García-Bustamante E, Valero F (2008) Surface wind regionalization in complex terrain. *J Appl Meteorol Climatol* 47:308–325
- Jiménez PA, Dudhia J, Navarro J (2011a) On the surface wind speed probability density function over complex terrain. *Geophys Res Lett* 38(L22):803. doi:10.1029/2011GL049,669
- Jiménez PA, Vilà-Guerau de Arellano J, González-Rouco JF, Navarro J, Montávez JP, García-Bustamante E, Dudhia J (2011b) The effect of heatwaves and drought on the surface wind circulations in the NE of the Iberian Peninsula during the summer of 2003. *J Clim* 24:5416–5422
- Jiménez PA, Dudhia J, González-Rouco JF, Navarro J, Montávez JP, García-Bustamante E (2012) A revised scheme for the WRF surface layer formulation. *Mon Wea Rev* 140:898–918
- Jiménez PA, González-Rouco J, Montávez J, Navarro J, García-Bustamante E, Dudhia J (2013) Analysis of the long-term surface wind variability over complex terrain using a high spatial resolution WRF simulation. *Clim Dyn* 40:1643–1656. doi:10.1007/s00,382-012-1326-z
- Kain JS, Fritsch JM (1990) A one-dimensional entraining/detraining plume model and its application in convective parameterization. *J Atmos Sci* 47:2784–2802
- Kain JS, Fritsch JM (1993) Convective parameterization for mesoscale models: the Kain-Fritsch scheme. In: Emanuel KA, Raymond DJ (eds) *The representation of cumulus convection in numerical models*. Meteorological monographs, vol 24. American Meteorological Society, pp 165–190
- Lange B, Larsen S, Hojstrup J, Barthelmie R (2004) The influence of thermal effects on the wind speed profile of the coastal marine boundary layer. *Bound Layer Meteorol* 112:587–617
- Levi Y, Shilo E, Setter I (2011) Climatology of a summer coastal boundary layer with 1290-MHz wind profiler and a WRF simulation. *J Appl Meteorol Climatol* 50:1815–1826
- Mass CF (1982) The topographically forced diurnal circulations of western Washington state and their influence on precipitation. *Bull Am Met Soc* 110:170–183
- Mlawer EJ, Taubman SJ, Brown PD, Iacono MJ, Clough SA (1997) Radiative transfer for inhomogeneous atmospheres: RRTM, a validated correlated-k model for the longwave. *J Geophys Res* 102:16663–16682
- Pena A, Gryning SE, Mann J (2010) On the length-scale of the wind profile. *Q J Roy Meteorol Soc* 136:2119–2131
- Pielke RA (2002) *Mesoscale meteorological modeling*. Academic Press, Amsterdam
- Sakazaki T, Fujiwara M (2008) Diurnal variations in summertime surface wind upon Japanese plains: hodograph rotation and its dynamics. *J Meteorol Soc Jpn* 86:787–803
- Sakazaki T, Fujiwara M (2010) Diurnal variations in lower-tropospheric wind over Japan part I: observational results using wind profiler network and data acquisition system (WINDAS). *J Meteorol Soc Jpn* 88:325–347
- Schröter JS, Moene AF, Holtslag AAM (2013) Convective boundary layer wind dynamics and inertial oscillations: the influence of surface stress. *Q J Roy Meteorol Soc* 139:1694–1771

- Shimada S, Ohsawa T, Chikaoka S, Kozai K (2011) Accuracy of the wind speed profile in the lower PBL as simulated by the WRF model. *SOLA* 7:109–112
- Simpson JE, Mansfield DA, Milford JR (1977) Inland penetration of sea-breeze fronts. *Q J Roy Meteorol Soc* 103:47–76
- Skamarock WC, Klemp JB, Dudhia J, Gill DO, Barker DM, Duda M, Huang XY, Wang W, Powers JG (2008) A description of the advanced research WRF version 3. Tech. Rep. TN-475+STR, NCAR
- Svensson G, Holtslag AAM (2009) Analysis of model results for the turning of the wind and related momentum fluxes in the stable boundary layer. *Bound Layer Meteorol* 132:261–277
- Tijm ABC, van Delden AJ (1999) The role of sound waves in sea-breeze initiation. *Q J Roy Meteorol Soc* 125:1997–2018
- Tijm ABC, Holtslag AAM, van Delden AJ (1999) Observations and modeling of the sea breeze with the return current. *Mon Wea Rev* 127:625–640
- van Delden A (1993) Observational evidence of the wave-like character of the sea breeze effect. *Beitr Phys Atmos* 66:63–72
- van Ulden AP, Wieringa J (1996) Atmospheric boundary layer research at cabauw. *Bound Layer Meteorol* 78:39–69
- Verkaik JW, Holtslag A (2006) Wind profiles, momentum fluxes and roughness lengths at Cabauw revisited. *Bound Layer Meteorol* 122:701–719
- Wichink Kruit RJ, Holtslag AAM, Tijm ABC (2004) Scaling of the sea-breeze strength with observations in The Netherlands. *Bound Layer Meteorol* 112:369–380
- Wieringa J (1989) Shapes of annual frequency distribution of wind speed observed on high meteorological masts. *Bound Layer Meteorol* 47:85–110